Journal of Molecular Structure 1380 (2027) 147409

Contents lists available at ScienceDirect

Journal of Molecular Structure

journal homepage: www.elsevier.com/locate/molstr

Luminescence lifetime up to microseconds in new coordination compounds with aminopyrazine and acetate

Meiry Edivirges Alvarenga [a], Ricardo Costa de Santana [b], Lauro June Queiroz Maia [b], Bárbara Júlia G. Dutra [a], Freddy Fernandes Guimarães [a], Felipe Terra Martins [c,*]

[a] Instituto de Química, Universidade Federal de Goiás, Goiania, GO, 74001-970, Brazil
[b] Instituto de Física, Universidade Federal de Goiás, Goiania, GO, 74001-970, Brazil
[c] Instituto de Química, Universidade Federal de Alfenas, Alfenas, MG, 37130-001, Brazil

ARTICLE INFO

Keywords:
Crystal structure
Photoluminescence
TD-DFT
Crystal packing
Ampyzcad

ABSTRACT

Aminopyrazine (ampyz) and cadmium acetate assemble into a potent blue light emitting one-dimensional coordination polymer upon UV excitation. Here we were devoted to the replacement of cadmium in this optical material given its environmental and human health drawbacks. Three new ampyz-based coordination compounds were prepared and elucidated structurally, and had their light emission investigated upon UV excitation. The dihydrate crystal form of the discrete compounds $[Co(ampyz)_2(AcO)_2(H_2O)_2]$ and $[Ni(ampyz)_2(AcO)_2(H_2O)_2]$ reveal to be isostructural themselves and to Zn^{2+} and Mn^{2+} versions thereof. Compound $[Ag(ampyz)(AcO)]_n(H_2O)_n$ assembles into polymeric one-dimensional coordination chains which are strongly bonded to each other through π…π interactions, hydrogen bonding and intermetallic bonds. Despite of their negligible emission power, their found luminescence lifetimes presented values up to 6 times greater than the previously reported parent complex, which can be correlated to the presence and strength of π…π stacking interactions. The Ag^+ compound has the shortest π…π interactions measuring 3.415 Å, with the emission lifetime in the μs order. However, these intermolecular contacts seem be responsible to quench the emission power together with intrinsic electronic features probed by TD-DFT. The electronic transitions responsible for UV excitation exhibit low oscillator strengths due to the orthogonality of the donor and acceptor orbitals, receiving significant metal *d* contribution besides enrolment of single-coordinated acetate ligand.

1. Introduction

The search for new materials able to emit visible light under excitation attracts much attention nowadays. This is mainly motivated by the impressive application of luminescence materials in current technology displays present in practically all electronic devices across worldwide society. In this way, less expensive, more sensitive and tuneable alternative materials can mean desired advances in much technological fields [1–10].

In the 2019 year, our research group reacted ampyz with cadmium acetate to produce one of the most efficient materials known up to that date to convert UV radiation into blue light [11]. Given the Cd environmental and human health drawbacks, we were interested to change it. Unfortunately, the Cd substitution for manganese and zinc keep the blue-light-emission from the ampyz coordination polymers upon UV excitation, but with much decreased efficiency compared to the Cd^{2+} inspirer [12,13]. In the case of Mn^{2+}, low-gap*D*-shaped HOMO-LUMO orbitals were found intercalating those responsible for UV absorption, producing low-frequency radiative decay what quenches the target luminescence [12]. Already in the Zn^{2+} coordination chains, the emission efficiency decreases as a result from the cleavage of one acetate coordination bond since Zn^{2+} is smaller than Cd^{2+} [13]. The absence of this coordination bond resulted in HOMO in the acetate rather than only in ampyz as occurs in the pioneer Cd^{2+}complex, which causes poor orbital overlap and lower structural rigidity, and then less efficient charge transfer and higher radiativeless decay.

Given the knowledge of luminescent properties of coordination compounds with cobalt, nickel and silver [7,14–18], we here reacted acetate salts thereof with ampyz in attempt to obtain high-efficiency blue light emitting coordination polymers similar to the Cd^{2+} precedent. In turn, we obtained two discrete coordination compounds of Co and Ni (compounds 1 and 2, respectively), while Ag^+ formed a

* Corresponding author.
E-mail address: felipe.martins@unifal-mg.edu.br (F.T. Martins).

https://doi.org/10.1016/j.molstruc.2026.147409
Received 7 July 2026; Received in revised form 31 July 2026; Accepted 21 August 2026
Available online 22 August 2026

coordination chain (compound 3) similar to the desired one, all them with emissions centred on 469 nm upon UV excitation. Such as the other zinc and manganese versions of our inspirer, quantum yields of found emissions are negligible and the reasons for this are presented here based on structural and electronic features.

2. Materials and methods

2.1. Synthesis

All reagents were acquired commercially and were used without further purification. All reactions were performed at room temperature (25 °C) upon magnetic stirring for 2 h of solutions prepared directly in ethanol (5 mL), using 10 mL penicillin-type vials. For synthesis of 1 and 2, the corresponding acetate salt tetrahydrate (25.0 mg, 0.1 mmol) and ampyz (19.0 mg, 0.20 mmol) were dissolved together, while equimolar amounts of silver acetate (16.7 mg, 0.1 mmol) and ampyz (9.5 mg, 0.1 mmol) were taken for synthesis of 3. After the stirring period, the vials were kept open for standing in the dark within a crystallization chamber, at 25 °C. Crystals suitably shaped for the single-crystal X-ray diffraction experiment were isolated from the mother solution after one week of solvent slow evaporation, while complete solvent evaporation was reached within ca. two weeks upon standing.

2.2. Single-crystal X-ray diffraction

Single-crystal X-ray diffraction data were acquired using a Bruker-AXS Kappa Duo diffractometer (APEX II CCD detector; Mo Kα beam, 296 K). Cell indexing and refinement and full intensity datasets processing were performed with Bruker programs SAINT and SADABS. All datasets were corrected for absorption phenomenon (Multi-scan) [19]. Structure solution and refinements were carried out using SHELXT and SHELXL [20], respectively, using the WinGX [21] software package. Structure interpretation and drawing were performed with Mercury [22]. Non-hydrogen and hydrogen atoms were treated in the refinements as anisotropic and isotropic, respectively. All CH hydrogens were positioned for bonding to their corresponding carbons according to expected valence angles and lengths, and their coordinates were not refined even though oscillating as changes in the parent carbon coordinates. All NH and water hydrogens were identified in the difference Fourier map and then constrained during refinements. The isotropic hydrogen displacement parameters were set to 1.2Uiso(C/N) or 1.5Uiso (O/C_{methyl}). The X-ray diffraction datasets are available for the three structures under CCDC deposit codes shown in Table 1, together with a crystal data summary.

Table 1
Summary of crystal data collected with MoKα at room temperature and refinement statistics for the three structures elucidated here.

	1	2	3
structural formula	$C_{12}H_{24}CoN_6O_8$	$C_{12}H_{24}NiN_6O_8$	$C_6H_{10}AgN_3O_3$
space group	*P*-1	*P*-1	*C*2/m
Z/*Z*'	1/0.5	1/0.5	4/0.5
a (Å)	7.0522(5)	7.0570(9)	18.6358(11)
b (Å)	8.3385(6)	8.2699(11)	7.1830(4)
c (Å)	9.5243(6)	9.5323(13)	6.9005(4)
α (°)	100.246(2)	99.826(3)	90
β (°)	106.968(2)	107.610(3)	106.883(2)
γ (°)	109.336(2)	109.789(3)	90
V (Å)^3	481.53(6)	475.24(11)	883.90(9)
θ range for data collection (°)	2.347–25.227	2.353–25.142	2.284–25.129
Completeness to θ_{max} (%)	99.0	100	99.4
data collected	10,725	12,932	7263
unique reflections	1721	1705	855
unique reflections with $I > 2s(I)$	1464	1287	571
symmetry factor (R_{int})	0.0786	0.1366	0.0587
parameters refined	124	125	73
goodness-of-fit on F^2	1.153	1.017	1.039
final *R1* factor for $I > 2s(I)$	0.0667	0.0512	0.0383
wR2 factor for all data	0.1796	0.1168	0.0887
largest Dr peaks (*e*/Å^3)	1.115/−1.035	0.378/−0.736	0.651/−0.851
CCDC deposit number	2571139	2571140	2571138

2.3. Optical measurements

Photoluminescence excitation and emission spectra were recorded at room temperature using a Horiba Jobin-Yvon Fluorolog spectrofluorometers, models FL3–221 and FL3–22, both equipped with Hamamatsu photomultiplier and dual monochromators, in which 450 W Xe lamps were used as an excitation source. A bandpass of 1.0 nm, increment of 0.5 nm, and integration times of 0.2 s were used for both emission and excitation measurements. Photoluminescence decay curves were recorded using pulsed NanoLeds with excitations at 290, 340, and 390 nm, and ~ 1 ns width pulses and 1 MHz frequency.

2.4. Computational details

The molecular models employed in all calculations consisted of isolated single molecules extracted from the crystal unit cell. Molecular geometries were fully optimized at the Density Functional Theory (DFT) level, adopting the crystallographic coordinates as initial geometries. Harmonic vibrational frequency calculations were subsequently performed on all optimized structures to confirm that each corresponds to a true minimum on the potential energy surface, as evidenced by the absence of imaginary frequencies. Vertical electronic transition energies and corresponding oscillator strengths were obtained for the 70 first transitions of the same symmetry by means of Time-Dependent DFT (TD-DFT) calculations. To simulate the UV–Vis absorption band profiles and to facilitate comparison with the experimental spectra, the discrete vertical electronic transitions were convoluted with Lorentzian functions with a Full Width at Half Maximum of 20 nm. All electronic structure calculations employed the MN15L exchange-correlation functional [23] in conjunction with the def2-SV(P) basis set [24,25], using the Gaussian 16 software package [26].

Global chemical reactivity descriptors were derived from the frontier molecular orbital energies of the highest occupied (HOMO) and lowest unoccupied (LUMO) molecular orbitals. The chemical potential (μ), chemical hardness (η), and electrophilicity index (ω) were calculated according to the following expressions [27]:

$$\mu = (E_{HOMO} + E_{LUMO})/2$$

$$\eta = (E_{LUMO} - E_{HOMO})/2$$

$$\omega = \mu_2/2\eta$$

3. Results and discussion

3.1. X-ray diffraction analysis

In this study, ampyz ligand gives rise to a discrete mononuclear coordination complex with either Co^{2+} or Ni^{2+}. Besides one transition metal ion, two monodentate acetate anions, two monodentate ampyz ligands and two coordinated water molecules are in the discrete complex molecule. Two non-coordinated water molecules are present per each coordination compound in the lattice, yielding a dihydrate crystal form of general formula $[M(ampyz)_2(AcO)_2(H_2O)_2]_2(H_2O)_2$ (M = Co^{2+} and Ni^{2+}). However, both asymmetric units have half of one coordination complex and one free water, being the second non-coordinated water molecule and the other molecular half generated by inversion symmetry. In fact, the centrosymmetry coincides with metal ion coordinates. Both metal ions are six-coordinated, with their square-pyramidal plane formed with two oxygens from each monodentate acetate and two ones

from water, while the axial positions are given by the heterocyclic nitrogen of each monodentate ampyz ligand (Fig. 1). Following this coordination pattern, amino groups are near to the non-coordinated azo nitrogens, lying away from acetate oxygens, becoming unavailable the intramolecular NH…O hydrogen bonding between these groups as occurs in the ampyz-metal polymeric chains. On contrary, free acetate oxygens are intramolecularly hydrogen bonded to coordinated water molecules. Besides being isostructural between them, these two complexes and their crystal forms have isostructural versions with Mn^{2+} [12] and Zn^{2+} [13]. Indeed, acetate salt of these two transition metal ions can form either this discrete compound or the polymeric chain depending on the crystallization solvent, which was not observed here with acetate salts of Co^{2+} and Ni^{2+}. In turn, $Cd^{2+}$is known to be coordinated by acetate and ampyz only into infinite one-dimensional chain thus far [11]. Bond lengths and angles around the metal ions are displayed in Tables S1 and S2 for the compounds elucidated here.

The crystal packing of these discrete coordination compounds is marked by one-dimensional chains in which translation-symmetry related molecules are held together through OH···N hydrogen bonds between coordinated water and the non-coordinated azo nitrogen of ampyz (see Fig. 1 and Table S3 for geometry of hydrogen bonds). When two molecules are positioned to assemble two of these reciprocal OH…N hydrogen bonds, they then stack on each other by means π…π contacts, with distances between the ampyz centroids of 3.618 Å and 3.627 Å in 1 and 2. In addition, another π…π contact is formed between ampyz rings of distinct packing chains (3.733 Å and 3.739 Å in 1 and 2), so that each ampyz ligand interacts by π…π above and below its ring, which can contribute to quench photoluminescence. In fact, the Cd^{2+} inspirer has not π…π interaction, not quenching therefore its radiative UV conversion into blue light. Furthermore, the non-coordinated water molecule binds at the side of chain near to acetate, to accept hydrogen bonding from amine group and to donate two ones to the coordinated and non-coordinated acetate oxygens belonging to distinct chains, acting as connecter between them as well as π…π contacts do.

Silver acetate has formed the expected coordination chain with ampyz. It has crystallized with half acetate, half Ag^{+} ion and half lattice water, all them laid on a mirror plane perpendicular to [010] (except for one full occupancy CH_3 hydrogen out of the mirror plane), and half ampyz with its NH_2 group owing 50% occupancy, which is therefore disordered over another sites set generated by the same mirror symmetry which completes the acetate, silver and water species. This is a monohydrate crystal form of general formula [Ag(ampyz)(AcO)](H_2O). Each metal ion is coordinated in line by two ampyz azo nitrogens, and by one acetate oxygen perpendicularly oriented relative to the fluorophore ligands, in a T-shaped geometry (N-Ag-N and N-Ag-O angles = 168.5º and 94.5º). The one-dimensional coordination polymer grows up therefore through the Ag-N bonds along the *b* axis, with high coplanarity between ampyz ligands (RMSD for the Ag(ampyz)$_2$ non-hydrogen atoms fitted on the l.s. plane is 0.0978 Å). Meanwhile, these planar chains are stacked on the top of each other along de *c* axis, through strong π…π interactions (this distance between ampyz centroids is green coloured in Fig. 2, having a short value of 3.415 Å), classical hydrogen bonds between amine group and the non-coordinated acetate oxygen, and intermetallic Ag-Ag bonds (Fig. 2). Such Ag…Ag separation is 3.228 Å, which is compatible with the formation of such a bond (see Tables S1 and S2 for the other bond lengths and angles around Ag^{+}). This interaction set gives rise to a pair of coordination chains kept strongly in contact, which are further π…π stacked on top of each other along the *c* axis (this distance between ampyz centroids is cyan coloured in Fig. 2, having a value of 3.543 Å). Silver trifluoroacetate also assemble a similar one-dimensional chain with ampzy (CSD reference code IWETAG) [28]. However, this is not isostructural with respect to ours reported here. Their unit cell parameters, space group and asymmetric unit contents (for IWETAG, a = 19.5083(18) Å, b = 6.9148(7) Å, c = 14.0530(14) Å, β=101.784(2)°, $C2/c$, Z' = ($C_6H_5AgF_3N_3O_2$)(H_2O)$_{0.5}$; see Table 1 for comparison with the corresponding values in 3) differ as a consequence of distinct architectures of the chains, as well as their disposition. In the literature compound, chains are not planar, with

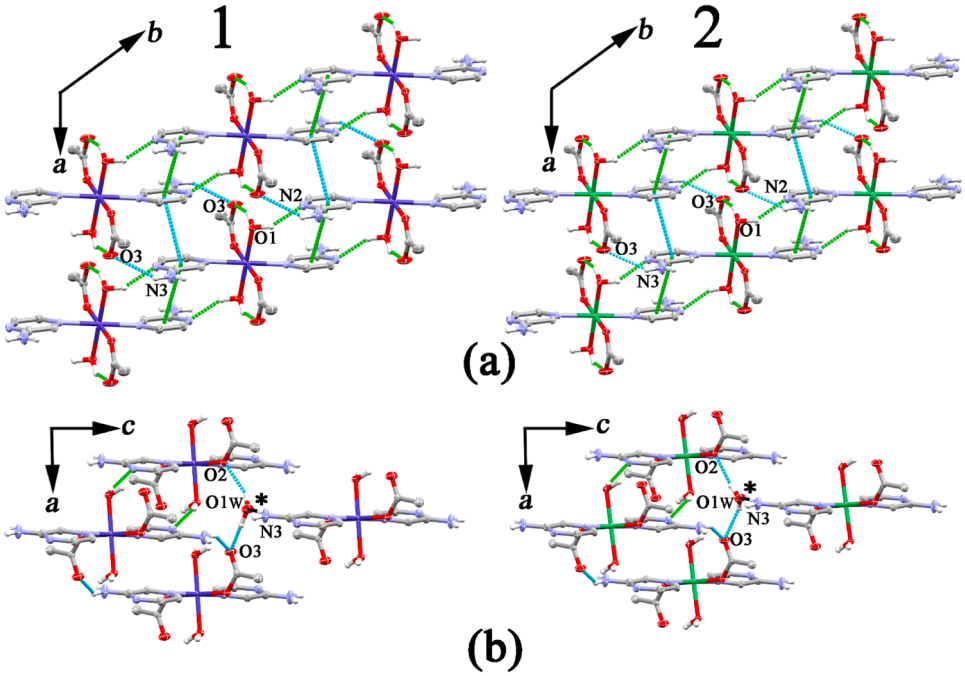

Fig. 1. Isostructural discrete coordination compounds made up of ampyz and Co (1) or Ni (2) acetate. 30% Probability ellipsoids draw non-hydrogen atoms, while NH and OH hydrogens are depicted as arbitrary radius spheres (CH hydrogens were omitted for sake of clarity). (a) Two chains grown along the *b* axis are stacked along the *a* axis on the top of each other through π…π stacking and aided by NH…O interactions. (b) The role of the non-coordinated water as hydrogen bonding donor to two chains stacked along the *a* axis and as acceptor from another one packed laterally along the *c* axis (π…π and intramolecular interactions were not drawn in this panel for clarity). Scheme of contacts colours (dashed lines): green, intramolecular (OH…O) and chain formation along the *b* axis (OH…N and π…π); cyan, packing of the chains along the *a* axis (NH…O, OH…O and π…π); black and asterisk marked, NH…O connecting the chains along the *c* axis.

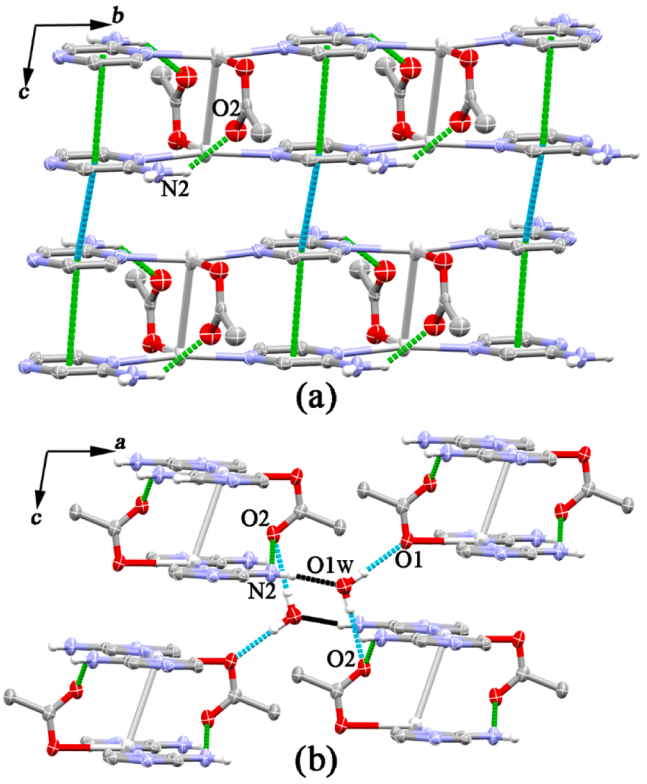

Fig. 2. Silver acetate assembles into an one-dimensional coordination chain with ampyz. 30% Probability ellipsoids draw non-hydrogen atoms, while NH and OH hydrogens are depicted as arbitrary radius spheres (CH hydrogens were omitted for sake of clarity). (a) The coordination chain growing along the *b* axis is stacked on the top of one another by means of π…π interactions. NH…O Hydrogen bonds and Ag_2 bonds help holding together two stacked coordination chains along the *c* axis, which are further stacked on another chains pair by through π…π interactions, and aided by hydrogen bonding donation from water to their acetate (shown in (b) together with the packing of the chains along the *a* axis through NH…O hydrogen bonding). Scheme of contacts colours (dashed lines): green, the formation of a pair of stacked coordination chains (NH…O and π…π); cyan, stacking of these chains pairs along the *c* axis (OH…O and π…π); black, NH…O connecting the chains along the *a* axis.

a wave-like array of the ampyz ligands (RMSD for the $Ag(ampyz)_2$ non-hydrogen atoms fitted on the l.s. plane is 0.273 Å) (Fig. S1). Consequently, these chains are not stacked directly on the top of each other as occurs in our structure. There is an offset of 1.44 Å between the ampyz centroids Cg, which sets the azo nitrogen in the line with the center of a stacked ampyz ring (N_{azo}…Cg = 3.484 Å) and displaces the Ag^+ ions by 4.1696(5) Å. Another difference is in the anion coordination geometry. The coordinated oxygen of trifluoroacetate is not so perpendicular to ampyz ligands, with two crystallographically independent N-Ag-O angles of 88.52(7)° and 104.37(7)°. This deviation from the N-Ag-N coordination environment hinder interaction between the anion and NH_2 group, while the non-coordinated anion oxygen is a hydrogen bonding acceptor from lattice water which connects non-stacked chains along the third crystallographic dimension through hydrogen bonding donation to trifluoroacetate and acceptation from NH_2. In our structure, such interactions between amine groups and water also connect non-stacked chains along the *a* axis, but water is hydrogen bonding donor to acetate oxygens of neighbouring chains pair stacked along the c axis (see Table S3 for geometry of hydrogen bonds).

3.2. Optical spectroscopy

In Fig. 3a, the diffuse reflectance spectrum (DR) for each studied compound is shown, which were acquired at room temperature in the range from 250 to 1800 nm. In the case of compound 3, the DR spectrum presented only a slight band in the 1420–1800 nm region, commonly assigned to third and second overtones of the aromatic C—H vibrations [29]. Both spectra of 1 and 2 presented this same absorption band viewed in the spectrum of 3, but much more intense, together another absorption at 1360–1410 nm region, attributed to overtones of the O—H stretching vibrations [29]. Also, DR spectra of 1 and 2 had broad absorption bands spread over all spectral range, typical of 3d metal ions. Particularly, the DR of 1 was present with a very broad absorption band in the 778 – 1434 nm range, centred at 1180 nm, which is generally interpreted as a transition from the ground state $^4A_2(F)$ to excited state $^4T_1(F)$, accomplished by other three small absorptions centred at 462, 469 and 523 nm, that are associated with transitions such as $^4T_1(F)$ to $^4T_1(P)$ of Co^{2+} [30,31]. Concerning to DR spectrum of 2, it also presents a broad band centred at 1053 nm, and two others at 626 and 432 nm. All of them are usually assigned to transitions from Ni^{2+} ground state $^3A_2(F)$ to excited states $^3T_2(F)$, $^3T_1(F)$, and $^3T_1(P)$, respectively [32].

Based on the DR spectra (Fig. 3a), in order to obtain the optical band gap (E_g) of the compounds, we have used the Kubelk-Munk [33] approach to construct the plots $[F(R_\infty)h\nu]^2$ vs. $h\nu$, where R_∞ is the ratio between the reflectance of the sample divided by the reference one ($R_{sample}/R_{reference}$), h is the Plank constant, and ν is the frequency, which, with the help of Tauc relation [34], $\alpha h\nu = A(h\nu - E_g)^{1/2}$, makes it possible to determinate the E_g by extrapolating the linear fitted region of the plot to $[F(R_\infty)h\nu]^2 = 0$. The values obtained are 3.34 eV for 1, 3.32 eV for 2, and 2.94 eV for 3, which are given in Table 2 together with those obtained for other previously reported metalo ampyz complexes for comparison. Fig. S2 shows the plots $[F(R_\infty)h\nu]^2$ vs. $h\nu$ for [Cd(ampyz)$(AcO)_2(H_2O)]_n$ [11] (4), [Zn(ampyz)$(AcO)_2(H_2O)]_n$ (5) [13], [Zn$(ampyz)_2(AcO)_2(H_2O)_2](H_2O)_2$ (6) [13], [Mn$(ampyz)_2(AcO)_2(H_2O)_2](H_2O)_2$ [12] (7), and for pure aminopyrazine (8) [12]. The E_g values indicate that all compounds can be considered as non-conducting materials. Moreover, all evaluated compounds present E_g values lower than that obtained for pure ampyz (8), following the trend: 8 > 5 > 1 ~ 2 > 6 > 4 > 7 ~ 3. In addition, it can be noted the E_g values of 3*d* ions are greater than that of 4*d* ion. This phenomenon is associated to the capability of 4*d* ions to create different electronic environments than 3d ions, due to their more diffuse *d*-orbitals and their resistance to change their ground state spin configuration when binding ligands [35–38]. In the case of 7, the lower obtained E_g value, can be due the high spin configuration of Mn^{2+} (S = 5/2). The band gap ceases to be a simple one-electron transition and begins to involve multiple excited states with different spin multiplicities, which can flatten the effective band gap in terms of molecular conductivity.

3.3. Photoluminescence

The normalized excitation and emission spectra for 1–3 compounds are shown in Fig. 4a-c, in which the maximum of emission band, λ_{emi}, was monitored for each sample at room temperature (see Table 3). The absorption spectrum of 1 presents only one well-defined absorption centred at ~ 325 nm, and a less pronounced band at 285 nm also reported for 7 [12]. The excitation spectra of 2 and 3 present some similarities, which consist of a sum of up to three bands among 250 to 350 nm. In the spectrum of 2, there are two well-defined two bands centred at 280 and 365 nm. In 3, a third band can be observed in the excitation spectrum as a band shoulder at 305 nm. Compounds 1–3 presented negligible PL quantum yields below 1%.

The normalized emission spectra of the compounds investigated here were acquired under some excitation energies, as shown in Fig. 4a-c. All of them consisted of a broad emission ranging among 350 and 600 nm. Independently of the used excitation energy, the maximum of the emission spectra for 2 and 3 remains at the same position, 384 and 391 nm, respectively. Moreover, all spectra present a second and wide emission band at ~469 nm, being more intense in 3. These profiles are quite similar to emission spectrum of 8 (pure ampyz molecule [12]).

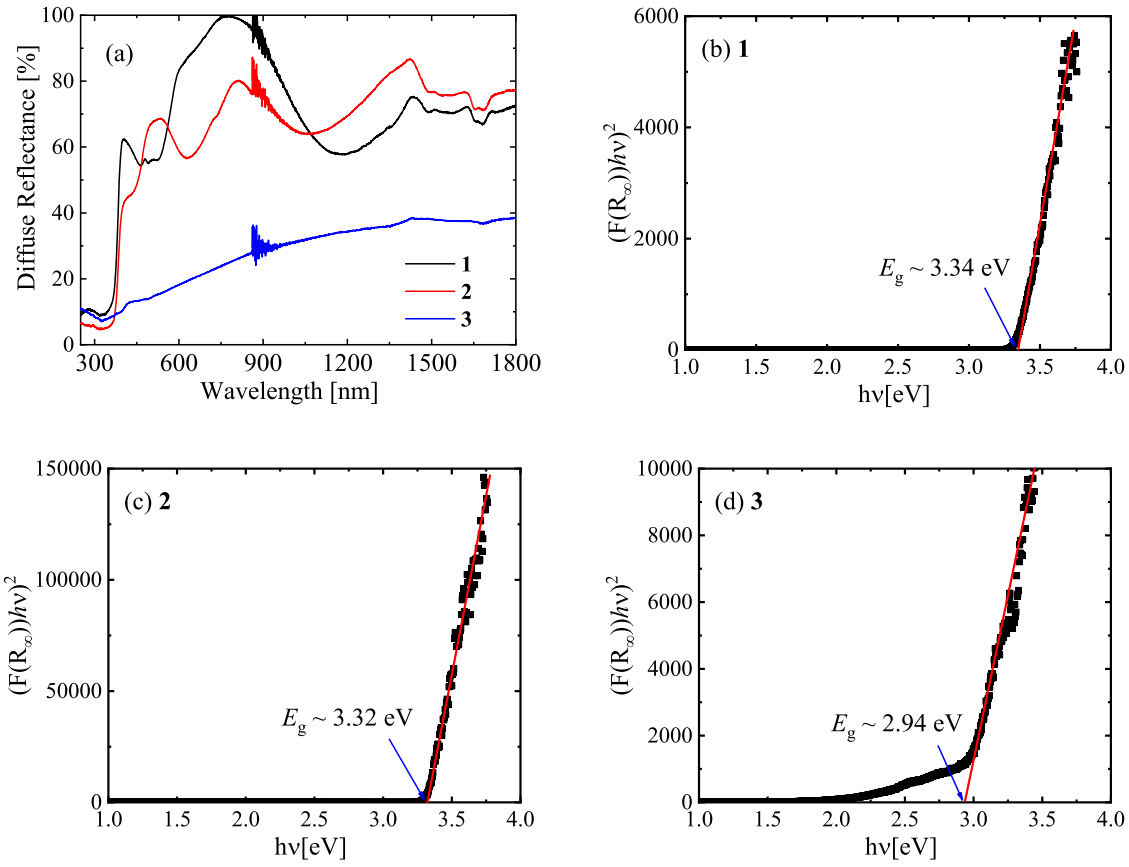

Fig. 3. (a) Diffuse reflectance spectra of 1, 2, and 3, (b) – (d) the plots of $(F(R_\infty)$ x $h\nu)^2$ versus photon energy for compounds 1, 2, and 3, respectively.

Table 2
Band gap E_g values for 1–8. (±0.05 eV).

Compound	E_g	Ref.
1	3.34	t.w.
2	3.32	t.w.
3	2.94	t.w.
4	3.14	[11]
5	3.51	[13]
6	3.20	[13]
7	2.98	t.w.
8	3.69	[12]

However, in the case of emission spectra of 1 (Fig. 4b), it can be noted that the maximum peak position depends on the excitation energy, standing at 392 and 405 nm for λ_{exc} = 325 and 365 nm, respectively, which is an indicative that the emission colour can be modulated. In addition, in Fig. 4d we can observe that the most intense emission of 3 exhibits a slight blue shift of 9 nm compared with emissions from 1 to 2, which have similar patterns and are overlapped. On the other hand, the emissions of 1, 2 and 3 display a slight blue shift compared to the emission of their parent complexes 4, 5, 6, and 7, and pure ampyz 8, whose emission peaks lies at 402, 400, 419, 410 and 410 nm, respectively, following the wavelength trend: 3 < 1 ~ 2 < 5 < 4 < 7 ~ 8 < 6.

The photometric parameters, the chromaticity coordinates (*x*,*y*) based on CIE 1931, the correlated colour temperature (CCT) and colour purity (CP) were also investigated for all compounds. Fig. 5 displays the (*x*,*y*) coordinates whose values are summarized in Table 3. Some peculiarities could be noted, for example, the (*x*,*y*) coordinates for 1 and 2 lies in the deep blue region of chromaticity diagram, having values near to those previously reported for other metal complexes (see Table 3). However, the colour coordinates obtained for 3 present a significative shift from deep blue to near white region of colour diagram, due to the broad and intense emission at ~469 nm, as shown in Fig. 4c. Also, we have calculated the colour purity (CP) in order to quantify the emission chromaticity behaviour of the studied complexes. The CP can be obtained by using the Eq. (1) [39]:

$$CP = \sqrt{\frac{(x-x_i)^2 + (y-y_i)^2}{(x_d-x_i)^2 + (y_d-y_i)^2}} \times 100\% \quad (1)$$

where (*x*,*y*) for each compound is given in Table 3. The pairs (x_d, y_d) = (0.150, 0.060) and (x_i,y_i) = (0.333, 0.333) are, respectively, the dominant wavelength point for blue colour and the colour coordinates and the standard white light. The found CP value for 1 sample, regardless of excitation energy, is 100%, while for 2 sample the CP depends on the excitation energy, varying from 100% for λ_{exc} = 280 nm, to 89.0% for λ_{exc} = 325 nm. These obtained values are in good agreement to those obtained for previously reported metal ampyz complexes (Table 3).

The calculated CCT values, were calculated with McCamy formula [40]: CCT = $449n^3 + 3601n^2 + 6823.3n + 5520.33$, where $n = (x - x_c)/(y - y_c)$, *x* and *y* being the chromaticity coordinates, and x_c = 0.3320 and y_c = 0.1858 the coordinates of chromaticity epicentre, and the calculated values are given in Table 3. For 1 and 2, the found values are in the range of 17,657 to 29,133 K, being compatible with those found for other metalo ampyz complexes 4, 5, 6, 7, and 8, whose values are respectively, 17,664, 21,114, 21,752, 21,539 and 36,380 K [11–13]. In contrast, the CCT value for 3 is 3796 K, being 4.6 times lower than that of 1, which finds explanation in the (*x*,*y*) coordinates of 3 to be closer to the white region of chromaticity diagram (see Fig. 5) than those of the other compounds.

The PL decay curves shown in Fig. 6 were taken at room temperature under excitation of 369 nm and monitoring the emission at 470 nm (see Table 4). The curves were best fitted with three-exponential functions

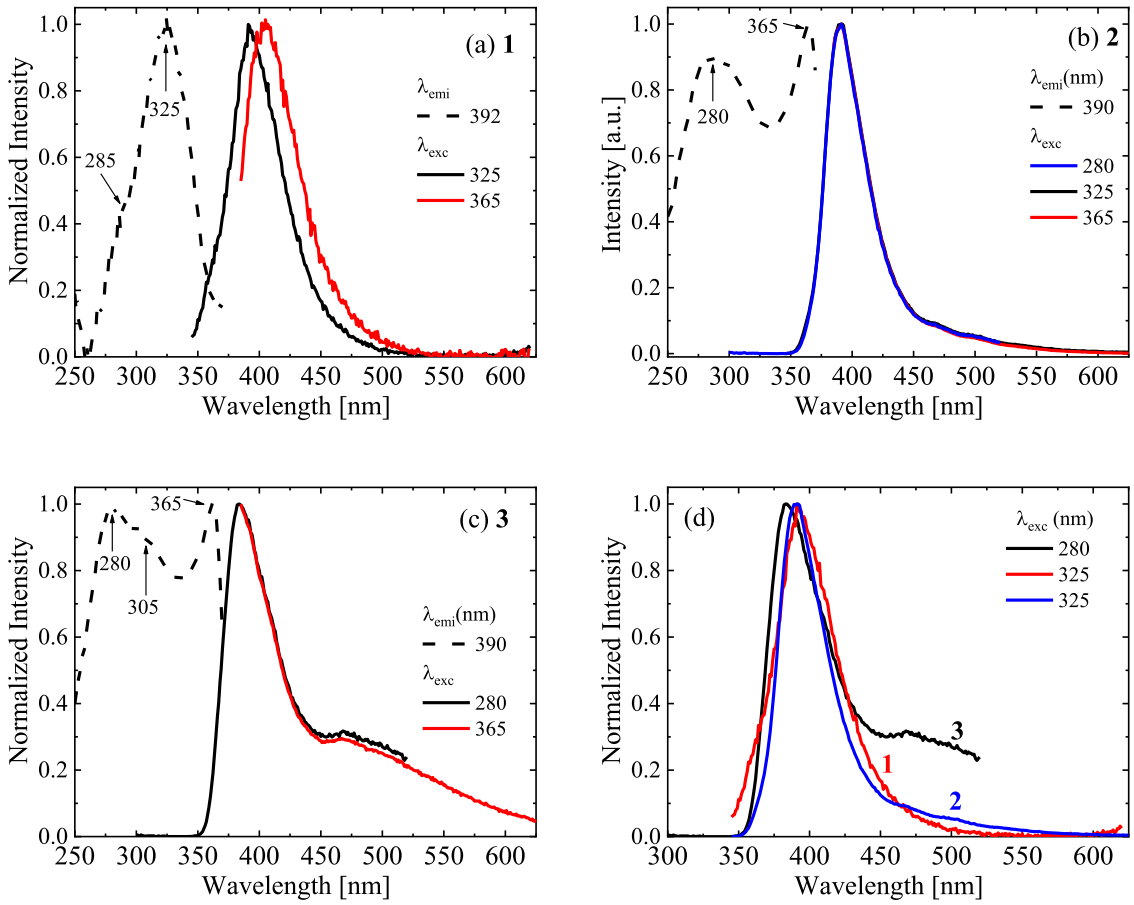

Fig. 4. Normalized excitation (dashed lines) and emission (solid lines) spectra of (a) 1, (b) 2, and (c) 3 samples. (d) a plot comparing the emissions of 1–3.

Table 3
Photometric parameters for 1–3 [λ_{exc} (in nm), CIE (*x*,*y*) chromaticity coordinates, colour purity (CP in %), and CCT values (in K)].

Compound	λ_{exc}	(*x*,*y*)	CP	CCT	Ref.
1	325	0.165, 0.032	100	17,657	t.w.
	365	0.158, 0.033	100	18,510	t.w.
2	280	0.149, 0.042	100	20,805	t.w.
	325	0.165, 0.087	89	29,133	t.w.
	365	0.160, 0.074	95	25,825	t.w.
3	280	0.211, 0.232	–	3796	t.w.
4	365	0.167, 0.037	100	17,664	[11]
5	330	0.158, 0.051	100	21,114	[13]
6	330	0.159, 0.055	100	21,752	[13]
7	370	0.158, 0.053	100	21,539	[12]
8	330	0.171, 0.105	79	36,380	[12]

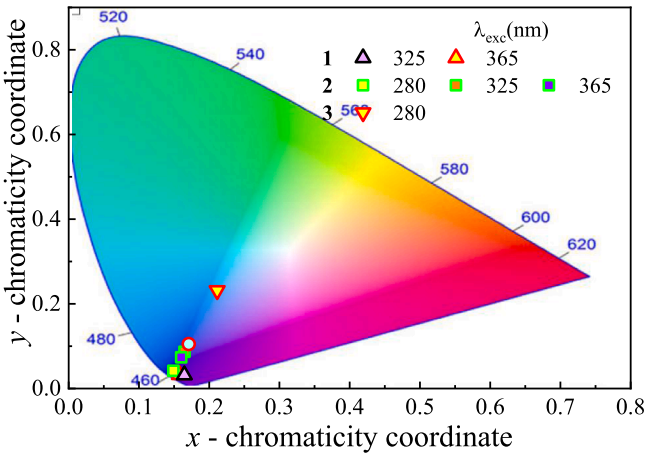

Fig. 5. CIE (x,y) coordinates for 1, 2, and 3.

as:

$$I(t) = I_0 + A_1\exp(-t/\tau_1) + A_2\exp(-t/\tau_2) + A_2\exp(-t/\tau_2) \quad (2)$$

where τ_1, τ_2 and τ_3 are lifetimes, which determine the decay rate for corresponding exponential components, and A_1, A_2 and are A_3 fitting parameters. The fitting line is presented in red in Fig. 6. The average lifetimes were calculated using the equation:

$$\tau_{AV} = \left(A_1\tau_1^2 + A_2\tau_2^2 + A_3\tau_3^2\right)/\left(A_1\tau_1 + A_2\tau_2 + A_3\tau_3\right) \quad (3)$$

The best obtained τ values presented in Table 4, with $\chi^2 = 0.987$, where it can be viewed similarities into the 1 - 3 lifetime values. All of them presented a fast τ value of ~ 1 ns, and a very low component ~264 ns for 1 and 2 and ~0.8 μs for 3, with average values of 24.58 ns, 23.65 ns, and 62.96 ns for 1, 2, and 3, respectively. Also, it can be noted that the values of 3d ions (Co and Ni) are similar, being almost 3 times lower than those obtained for 4d ion (Ag). Similar behaviour was observed for those report the 4d Cd ion (4), and the 3d ions Zn (5 and 6), and Mn (7) (see Table 4). A good correlation was observed between lifetimes and structural characteristics of the compounds. For example, compounds 1 - 3 have π...π stacking interactions, a feature which is not present in 4 to 8. However, these interactions occur between free discrete coordination molecules in 1 and 2, while they act between one-dimensional infinite chains in 3. Besides a rigidity gain in the former

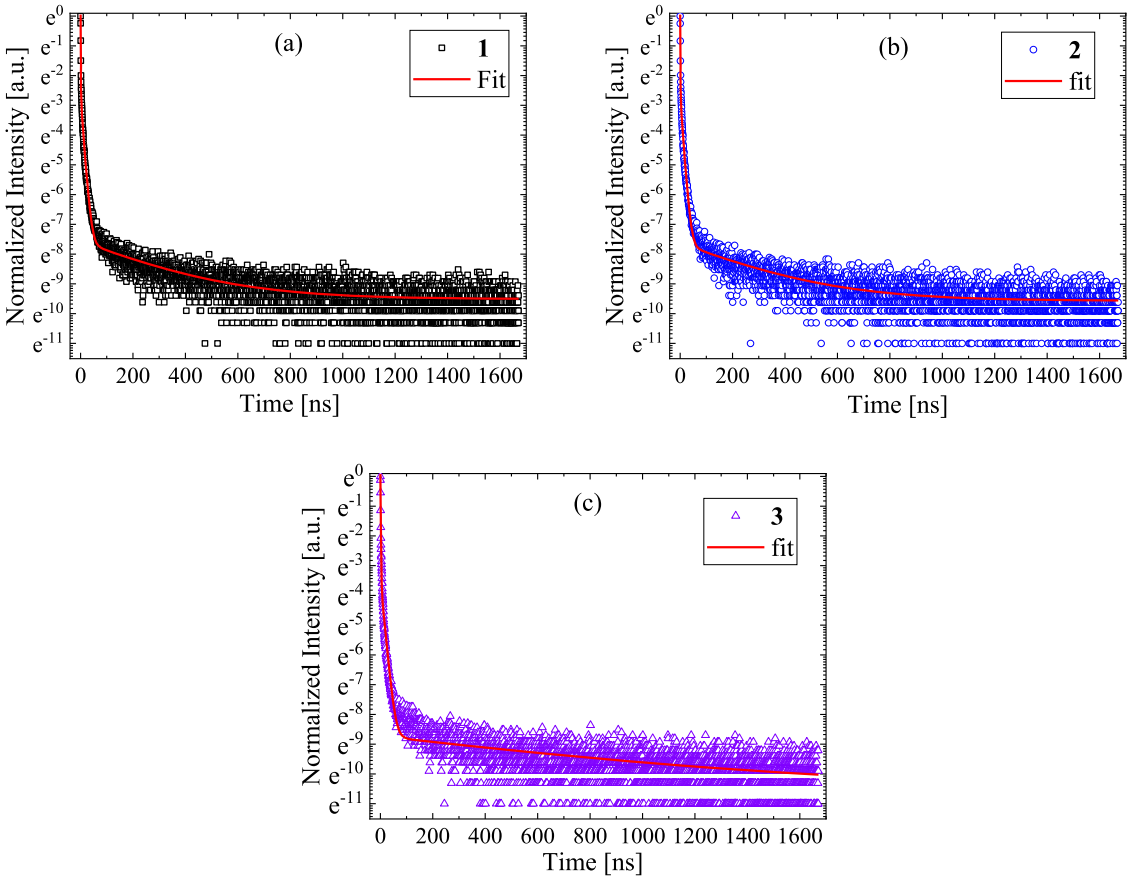

Fig. 6. Normalized emission decay curves of 1–3.

Table 4
Experimental lifetimes τ (in ns) of the fitted decay curves for 1–3 (λ_{exc} and λ_{emis} in nm).

Compound	λ_{exc}	λ_{emi}	τ_1	τ_2	τ_3	τ_{av}	A_1 (%)	A_2 (%)	A_3 (%)	Ref.
1	369	470	8.86	0.99	263.51	24.58	35.3	56.7	8.0	t.w.
2	369	470	8.70	0.84	265.32	23.65	35.3	57.2	7.5	t.w.
3	369	470	10.97	1.07	832.73	62.96	21.3	71.5	7.2	t.w.
4	365	402	10.04	190	–	9.92	92.96	7.04	–	[11]
5	330	400	9.33	5.98	8.64	5.74	99.99	0.008	0.001	[13]
6	330	419	2.23	–	–	2.23*	100	–	–	[13]
7	370	410	3.22	–	–	3.22*	100	–	–	[12]
8	330	410	0.88	–	–	0.88*	100	–	–	[12]

*Obtained from the integrated area of decay curves.

structure from its interconnected polymeric chain, the π…π interactions are notably stronger there than in 1 and 2, as afore discussed on the basis of the shorter separation between ampyz centroids in 3 than in 1 and 2. The presence of π…π stacking, in general, diminishes the movement degree of the molecules, which minimizes the energy loss by lattice phonons (non-radiative decay) increasing the emission lifetimes [41, 42], or even promoting the formation of new excited species, excimers, that generally possess forbidden electronic transitions due to symmetry or charge transfer states, resulting in slower radiative decay [43] and increasing the emission lifetime as observed in 1, 2 and, mainly in 3. On the other hand, these same stacking interactions are well known to deplete the emission efficiency [44], being a possible cause for negligible QY of 1–3.

3.4. Theoretical approach

The superposition of the experimental crystallographic and the theoretical DFT/MN15L/def2-SV(P)-optimized geometries is depicted in Fig. 7 for compounds 1, 2, and 3. The RMSD value for each superposition is in Table 5. As can be seen from this picture and this Table (all RMSD were values lower than 0.6 Å), confirming a close correspondence between the experimental and theoretical geometries. The frontier molecular orbital energies (HOMO and LUMO) and computed chemical reactivity descriptors are also reported Table 5.

Fig. 8 presents the theoretical TD-DFT UV–Vis absorption spectra of compounds 1, 2, and 3, computed for both the crystallographic (black lines) and the DFT/MN15L/def2-SV(P)-optimized geometries (red lines). The discrete vertical electronic transitions (oscillator strengths as a function of wavenumber) were convoluted with Lorentzian functions to simulate continuous band profiles comparable to the experimental spectra. Despite of the low RMSD values between the crystallographic and DFT-optimized geometries (Table 5), some differences are observed in the corresponding TD-DFT spectra, particularly in the low-energy region associated with transitions between the frontier molecular

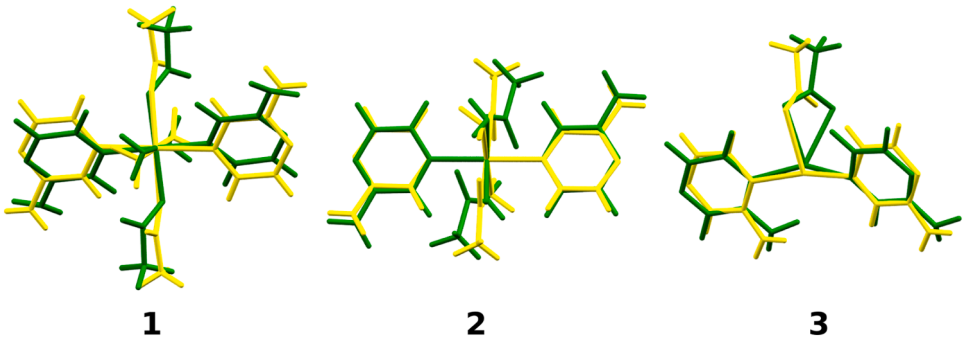

Fig. 7. Superposition of the experimental crystallographic (yellow) and the DFT/MN15L/def2-SV(P)-optimized geometries (green) for 1, 2 and 3.

Table 5
Root mean square deviation (RMSD, in Å) between the crystallographic and the DFT/MN15L/def2-SV(P)-optimized molecular geometries. Frontier molecular orbital energies (HOMO and LUMO), and global chemical reactivity descriptors: chemical potential (μ), chemical hardness (η), and electrophilicity index (ω) for 1, 2, and 3, all them reported in eV.

Compound	RMSD	E_{HOMO}	E_{LUMO}	μ	η	ω
1	0.5713	−4.061	−2.431	−3.246	0.815	6.464
2	0.5193	−4.360	−2.558	−3.459	0.901	6.641
3	0.3785	−4.736	−2.285	−3.510	1.226	5.027

orbitals. All three compounds exhibit uniformly low oscillator strengths in this region, consistent with the forbidden or nearly forbidden character of the frontier orbital transitions. Among the three compounds, the smallest oscillator strengths for both the crystallographic and optimized geometries were found for 2. Compounds 1 and 2 display comparable maximum oscillator strengths when computed from the crystallographic geometry, whereas for the optimized geometry, compound 3 exhibits a larger oscillator strength in the region around 280 nm relative to the other two compounds.

The trend of crystallographic geometries yielding larger oscillator strengths for the frontier orbital transitions compared to those obtained from the gas-phase optimized structures was observed. This finding suggests that the molecular geometry distortions induced by intermolecular interactions in the crystal lattice, such as hydrogen bonding and crystal packing forces, can partially lift the symmetry restrictions that render these transitions forbidden in the isolated single-molecule model, thereby enabling electronic transitions that are otherwise symmetry-forbidden in the gas phase.

The TD-DFT results compiled in Tables S4-S9 for the DFT/MN15L/def2-SV(P) optimized molecular geometries reveal that the lowest-energy electronic transitions are forbidden or nearly forbidden for all three compounds, as reflected by their uniformly low oscillator strengths. For compound 1, all transitions HOMO α (105α)→LUMO α (106α), HOMO−1 α /HOMO β (104α/104β)→LUMO+1 α /LUMO+2 β (106α–107β) present vanishing oscillator strengths ($f = 0.0000$) for both the crystallographic and optimized geometries. The remaining low-energy transitions, HOMO−1 β (104β)→LUMO β (105β), HOMO α (105α)→LUMO+1 α (107α), and HOMO−1 β (103β) → LUMO β (105β), yield oscillator strengths no greater than $f = 0.07$, confirming their forbidden character. For compound 2, the HOMO→LUMO and HOMO−1→LUMO transitions are forbidden ($f = 0.0000$) for both geometries. The HOMO→LUMO+1 and HOMO−1→LUMO+1 transitions exhibit oscillator strengths no greater than $f = 0.02$, which is below the threshold of practical optical significance. In compound 3 all four low-energy transitions (HOMO (75)→LUMO (76), HOMO (75)→LUMO+1 (77), HOMO−1 (74)→LUMO (76), and HOMO−1 (74)→LUMO+1 (77)) present oscillator strengths not exceeding $f = 0.019$, consistent with their forbidden or nearly forbidden excitation transitions. Taken together, these results indicate that the lowest-energy transitions in all three compounds are optically weak, and that the absorption features observed experimentally arise from higher-energy transitions with more significant oscillator strengths, as discussed above.

The frontier molecular orbitals HOMO−1, HOMO, LUMO, and LUMO+1 for the three studied compounds are depicted in Fig. 9. Transitions involving these orbitals often have favourable properties that can make them intense. However, for these compounds the oscillator strengths are low in absolute magnitude, which explains the negligible emission power of the compounds. Even if excitation initially goes to a higher allowed state (i.e., S0→S2, strongly allowed), the molecule rapidly relaxes with S2→S1(internal conversion). Then emission occurs from S1→S0 at negligible intensity.

Compounds 2 and 3 are closed-shell singlet species, and therefore their α and β spin orbitals are identical. Compound 1, in contrast, is an open-shell doublet, exhibiting distinct α and β frontier orbitals. Compound 1, with an open-shell electronic structure, has distinct α and β spin orbital manifolds. The HOMO−1 β orbital is essentially a pure metal d_{xz} orbital, while both HOMO−1 α and HOMO β orbitals exhibit mixed metal–ligand character, combining the metal d_{xy} orbital with oxygen p orbitals from the single-coordinated acetate ligand. In the cadmium inspirer, acetate ligand does not participate in these orbitals, since both of its oxygens are coordinated to the metal ion [11]. The HOMO α orbital presents contributions from the metal d_{z^2} orbital mixed with oxygen p orbitals of the coordinated water molecule. The LUMO α has a mixed character involving the metal $d_{x^2-y^2}$ orbital and p orbitals from both nitrogen and oxygen atoms of the ligand framework, while the LUMO β and LUMO+1 α and β orbitals are π antibonding orbitals localized over the ampyz ligands. The transitions from HOMO−1 α and HOMO α to the LUMO α orbital exhibit low oscillator strengths due to the orthogonality of the donor and acceptor orbitals, both symmetry-forbidden, as they involve excitations between orthogonal molecular orbitals with significant metal atomic d contributions. The transitions to the LUMO+1 α orbital, as well as all transitions involving the LUMO β and LUMO+1 β orbitals, have metal-to-ligand charge transfer (MLCT) character, involving electron redistribution from metal$D$-type orbitals to the π* antibonding orbitals of the ampyz ligands, which accounts for their reduced oscillator strengths.

For compound 2, the HOMO−1 presents a mixed metal–ligand character, arising from the interaction between the metal d_{xy} orbital and the oxygen p orbitals of the acetate ligand, in a similar way occurring in 1. The HOMO is also made of mixed character, combining the metal d_{z^2} orbital with oxygen p orbitals from the coordinated water molecule. The LUMO displays contributions from the metal $d_{x^2-y^2}$ orbital mixed with oxygen and nitrogen p orbitals of the ligands, while the LUMO+1 is a π antibonding orbital largely localized over the ampyz ligands. The low oscillator strengths observed for the HOMO−1/HOMO → LUMO+1 transitions in compound 2 are consistent with their MLCT character, involving electron density redistribution from orbitals with predominant metal d character to the π* antibonding orbital of the ampyz ligand. The HOMO/HOMO−1→LUMO transitions carry significant metal d character and therefore they are symmetry-forbidden, similarly to that

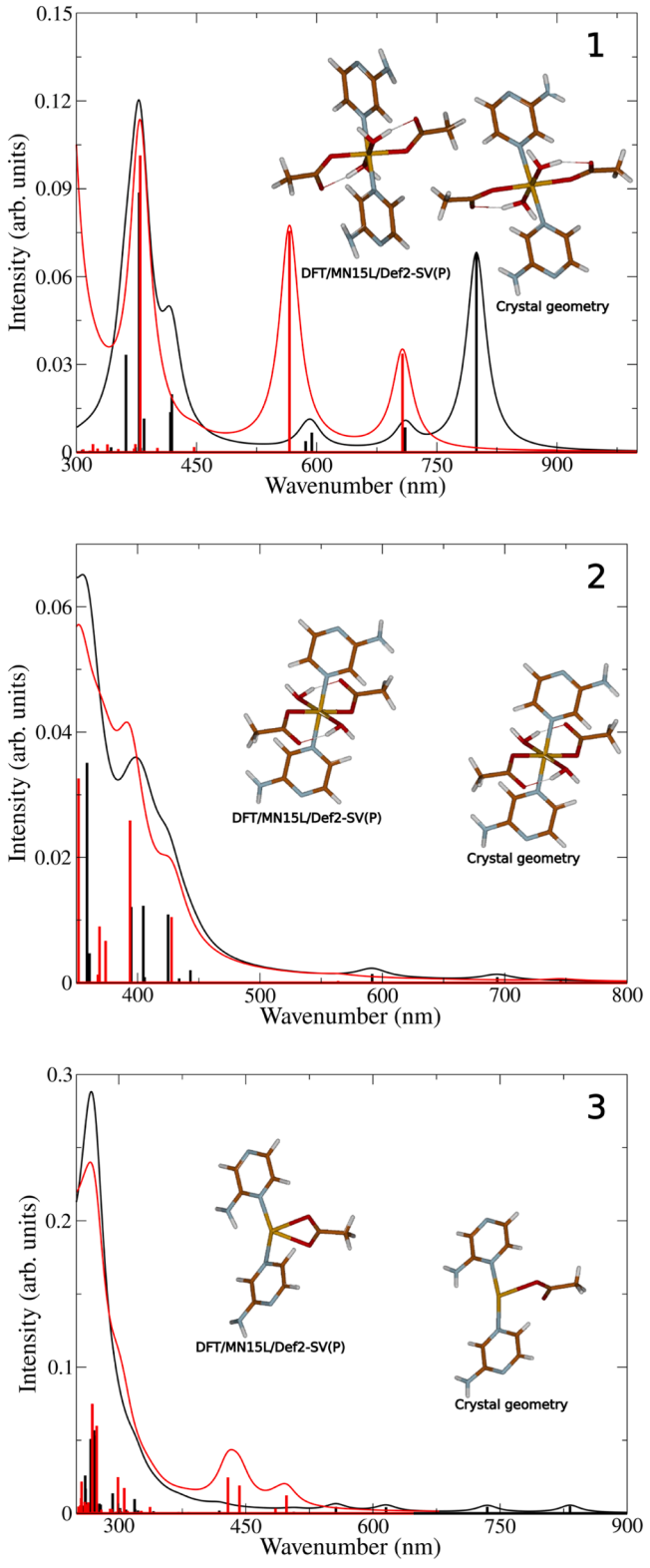

Fig. 8. Theoretical UV–Vis absorption spectra of compounds 1, 2, and 3, computed at the TD-DFT/MN15L/def2-SV(P) level. The calculated oscillator strengths (vertical bars) were convoluted with Lorentzian functions to reproduce the band shape of the experimental spectra. Black lines correspond to spectra obtained from the crystallographic molecular geometries; red lines correspond to spectra obtained from the DFT-optimized ones. Inputted (crystal geometry) and outputted (TD-DFT/MN15L/def2-SV(P)) molecular geometries are depicted in the panels.

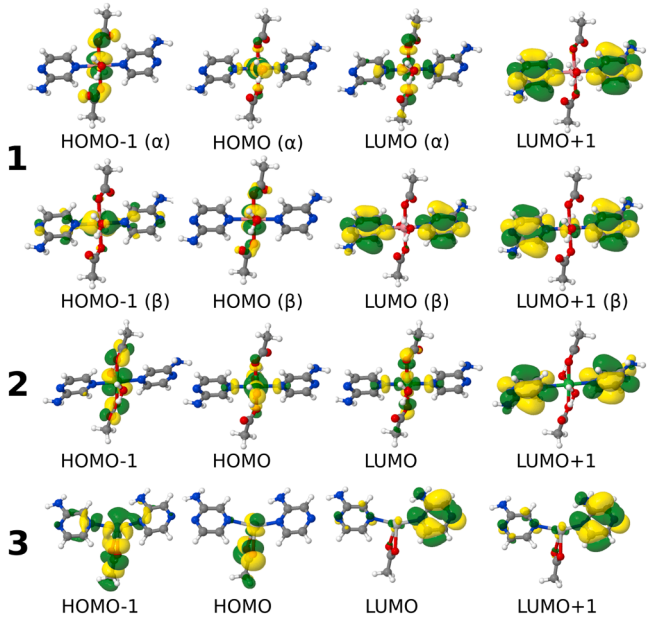

Fig. 9. Spatial distribution of the frontier molecular orbitals HOMO−1, HOMO, LUMO, and LUMO+1 for compounds 1, 2, and 3, computed at the DFT/MN15L/def2-SV(P) level. Isovalue = 0.025 au the colours green and yellow depict the distinct phases of the wave function.

observed in its isostructural compound 1.

In compound 3, the HOMO−1 is composed of mixed character, combining the metal d_{z^2} orbital with *p* orbitals from both the oxygen and carbon atoms of the acetate ligand. The HOMO presents contributions from the metal d_{xy} orbital mixed with oxygen *p* orbitals of the acetate ligand. Both the LUMO and LUMO+1 are closely related in character, each being a π* antibonding orbital localized over one of the ampyz ligands. The low oscillator strengths of the HOMO→LUMO and HOMO−1→LUMO transitions in compound 3 are consistent with their MLCT character, involving electron redistribution from orbitals with predominant metal *d* character (HOMO−1) or mixed metal *d*/oxygen *p* character (HOMO) to the π* antibonding orbitals of the ampyz ligands (LUMO and LUMO+1).

4. Conclusions

In this study, we have prepared three new ampyz-based coordination compounds. The dihydrate crystal form of the discrete compounds [Co(ampyz)$_2$(AcO)$_2$(H$_2$O)$_2$] and [Ni(ampyz)$_2$(AcO)$_2$(H$_2$O)$_2$] reveal to be isostructural themselves and to Zn^{2+} and Mn^{2+} versions thereof. Compound [Ag(ampyz)(AcO)]$_n$(H$_2$O)$_n$ assembles into polymeric coordination chain which is strongly bonded to each other through π…π interactions, hydrogen bonding and intermetallic bonds. The found luminescence lifetimes of 1–3 present values up to 6 times greater than the previously reported parent complexes, which can be due the presence of π…π stacking, whose strength correlates well with lifetime. The Ag^{+} compound has the shortest π…π interactions measuring 3.415 Å, with the emission lifetime in the μs order. However, these intermolecular contacts seem be responsible to quench the emission efficiency. Added to this intermolecular feature, the electronic transitions responsible for UV excitation exhibit low oscillator strengths due to the orthogonality of the donor and acceptor orbitals, receiving significant metal *d* contribution besides enrolment of single-coordinated acetate ligand. These results reinforce the fine balance of structural features need to high-efficiency emitters based on ampyz and transition metal ions, which go much beyond the molecular signature of the ligand and the metal to be coordinated, demonstrating the crucial role of secondary bonds such as π…π stacking.

Funding sources

This study was financed by the Brazilian agencies: Conselho Nacional de Desenvolvimento Científico e Tecnológico (CNPq) (427164/2018-4, 440225/2021-3, and 406441/2023-5), Coordenação de Aperfeiçoamento de Pessoal de Nível Superior (CAPES) – Finance Code 001 (AUGM 88881.004658/2024-01), Financiadora de Estudos e Projetos (FINEP), Fundação de Amparo à Pesquisa do Estado de Goiás (FAPEG), Centro de Excelência em Hidrogênio e Tecnologias Energéticas Sustentáveis (CEHTES), and Fundação de Apoio à Pesquisa (FUNAPE). The authors acknowledge Sistema Nacional de Fotônica (Sisfóton) – LIFóton / MCTi (440225/2021-3), Brazilian National Institutes of Science and Technology (INCTs), INCT-INFO (National Institute of Photonics) (409174/2024-6), and CNPq research fellowships awarded to RCS (CNPq/FAPEG 202510267001607), LJQM (304464/2025-2), CMS (#309922/2023-2), and FTM (#307074/2023-4).

CRediT authorship contribution statement

Meiry Edivirges Alvarenga: Methodology, Investigation. **Ricardo Costa de Santana:** Writing – review & editing, Methodology, Investigation. **Lauro June Queiroz Maia:** Writing – review & editing, Methodology, Investigation. **Bárbara Júlia G. Dutra:** Visualization, Validation, Methodology. **Freddy Fernandes Guimarães:** Writing – review & editing, Methodology, Investigation, Formal analysis. **Felipe Terra Martins:** Writing – review & editing, Writing – original draft, Visualization, Validation, Methodology, Investigation, Formal analysis, Conceptualization.

Declaration of competing interest

The authors declare that they have no known competing financial interests or personal relationships that could have appeared to influence the work reported in this paper.

Supplementary materials

Supplementary material associated with this article can be found, in the online version, at doi:10.1016/j.molstruc.2026.147409.

Data availability

Data will be made available on request.

References

[1] Z. Sun, Y. Zhang, X. Zhu, J. Yang, W. Xiao, Triple dynamic networks integrating robust mechanics, rapid self-healing, and tunable luminescence via lanthanide coordination, Sens. Actuators B Chem. 465 (2026) 140150, https://doi.org/10.1016/j.snb.2026.140150.

[2] Z. Yan, T. Liu, L. Ding, Y. Fang, Small organic molecule-based multicolor fluorescent smart materials: from design principles and optical properties to versatile applications, ACS Cent. Sci. 12 (2026) 751–765, https://doi.org/10.1021/acscentsci.6c00693.

[3] S. Ponmalakunnu, M.S.K. Kunjumohammed, A. Kadavangattil, S.N. Remello, S. Mathai, Exploring the multifunctional elegance of novel phenothiazine-based D-π-A fluorophores: solvatochromism, dual state emission and mechanochromic luminescence, J. Mol. Struct. 1369 (2026) 146383, https://doi.org/10.1016/j.molstruc.2026.146383.

[4] K. Shao, Q. Dong, Y. Meng, J. Chen, H. Wen, X. Wang, Z. Pan, S. Ye, J. Wang, Electron donor–acceptor alignment in matrix-engineered carbon dots for minute-scale persistent luminescence, Adv. Opt. Mater. 14 (2026) e71252, https://doi.org/10.1002/adom.71252.

[5] T. Mochimaru, T. Ogawa, T. Honda, K. Segawa, T. Wakabayashi, Y. Harakawa, T. Yoshida, K. Miyata, K. Onda, Optimized octahedral geometry and hidden rigidity of a mer-tridentate N-heterocyclic carbene ligand enhance luminescence of an Fe (III) complex, J. Am. Chem. Soc. 148 (2026) 26878–26889, https://doi.org/10.1021/jacs.6c08685.

[6] A. Slodek, M. Filapek, E. Schab-Balcerzak, M. Grucela, S. Kotowicz, H. Janeczek, K. Smolarek, S. Mackowski, J.G. Malecki, A. Jedrzejowska, G. Szafraniec-Gorol, B. M. Chrobok, S. Krompiec, M. Matussek, Highly luminescence anthracene derivatives as promising materials for OLED applications, Eur. J. Org. Chem. 2016 (2016) 4020–4031, https://doi.org/10.1002/ejoc.201600532.

[7] R-W. Huang, Y.-S. Wei, X.-Y. Dong, X.-H. Wu, C.-X. Du, S.-Q. Zang, T.C.W. Mak, Hypersensitive dual-function luminescence switching of a silver-chalcogenolate cluster-based metal–organic framework, Nat. Chem. 9 (2017) 689–697, https://doi.org/10.1038/nchem.2718.

[8] Y. Zhang, W.-Q. Liao, D.-W. Fu, H.-Y. Ye, C.-M. Liu, Z.-N. Chen, R.-G. Xiong, The first organic–inorganic hybrid luminescent multiferroic: (Pyrrolidinium)$MnBr_3$, Adv. Mater. 27 (2015) 3942–3946, https://doi.org/10.1002/adma.201501026.

[9] T. Mutai, H. Satou, K. Araki, Reproducible on–off switching of solid-state luminescence by controlling molecular packing through heat-mode interconversion, Nat. Mater. 4 (2005) 685–687, https://doi.org/10.1038/nmat1454.

[10] V.W.-W. Yam, K.K.-W. Lo, Luminescent polynuclear d10 metal complexes, Chem. Soc. Rev. 28 (1999) 323–334, https://doi.org/10.1039/a804249g.

[11] J.A. do Nascimento Neto, A.K.S.M. Valdo, C.C. da Silva, F.F. Guimarães, L.H.K. Q. Júnior, L.J.Q. Maia, R.C. de Santana, F.T. Martins, A blue-light-emitting cadmium coordination polymer with 75.4% photoluminescence quantum yield, J. Am. Chem. Soc. 141 (2019) 3400–3403, https://doi.org/10.1021/jacs.8b13561.

[12] M.A. Lemes, J.A. do Nascimento Neto, F.F. Guimarães, L.J.Q. Maia, R.C. de Santana, F.T. Martins, Isostructural coordination chains assembled with aminopyrazine: decreasing photoluminescence yield by Cd(II) replacement for Mn (II), J. Mol. Struct. 1236 (2021) 130352, https://doi.org/10.1016/j.molstruc.2021.130352.

[13] J.H.D. Campos, M.E. Alvarenga, M.A. Lemes, J.A. do Nascimento Neto, F. F. Guimarães, L.J.Q. Maia, R.C. de Santana, F.T. Martins, The critical role of the coordination sphere in the high-efficiency blue-light emission from aminopyrazine metal-organic polymers, Dyes Pigm. 186 (2021) 109025, https://doi.org/10.1016/j.dyepig.2020.109025.

[14] H. Wang, L. Fu, G.-H. Cui, New robust 2D cobalt(II) coordination polymer as an effective turn-on luminescent sensor to detect tb^{3+} and pefloxacin, J. Mol. Struct. 1316 (2024) 139025, https://doi.org/10.1016/j.molstruc.2024.139025.

[15] M. Beliaeva, A. Belyaev, H. Korhonen, O. Mrózek, J. Jänis, A. Steffen, I. O. Koshevoy, Acid–base interactions in luminescent silver(I) and gold(I) complexes with phosphine–phosphinate/phosphinite ligands, Inorg. Chem. Front. 13 (2026) 511–524, https://doi.org/10.1039/d5qi01622c.

[16] A. Cruz-Galván, J. Bucio-Ortega, J. Olguín, Complexes of Fe(II), Ni(II), and Zn(II) with a tetradentate naphthalene diimine−dipyrazole ligand: influence of a metal ion and anions on the luminescence properties, Cryst. Growth Des. 25 (2025) 4466–4480, https://doi.org/10.1021/acs.cgd.5c00374.

[17] J. Li, H. Ren, J. Li, L. Wang, Synthesis and fluorescent characteristics study of two novel Co(II) complexes, J. Fluoresc. 34 (2024) 2737–2743, https://doi.org/10.1007/s10895-023-03488-6.

[18] N. Lei, W. Li, D. Zhao, W. Li, X. Liu, L. Liu, J. Yin, M. Muddassir, R. Wen, L. Fan, A bifunctional luminescence sensor for biomarkers detection in serum and urine based on chemorobust nickel(II) metal-organic framework, Spectrochim. Acta Part A Mol. Biomol. Spectrosc. 306 (2024) 123585, https://doi.org/10.1016/j.saa.2023.123585.

[19] L. Krause, R. Herbst-Irmer, G.M. Sheldrick, D. Stalke, Comparison of silver and molybdenum microfocus X-ray sources for single-crystal structure determination, J. Appl. Crystallogr. 48 (2015) 3–10, https://doi.org/10.1107/S1600576714022985.

[20] G.M. Sheldrick, Crystal structure refinement with SHELXL, Acta Crystallogr. C Struct. Chem. 71 (2015) 3–8, https://doi.org/10.1107/S2053229614024218.

[21] L.J. Farrugia, WinGX and ORTEP for Windows: an update, J. Appl. Crystallogr. 45 (2012) 849–854, https://doi.org/10.1107/S0021889812029111.

[22] C.F. Macrae, I. Sovago, S.J. Cottrell, P.T.A. Galek, P. McCabe, E. Pidcock, M. Platings, G.P. Shields, J.S. Stevens, M. Towler, P.A. Wood, Mercury 4.0: from visualization to analysis, design and prediction, J. Appl. Crystallogr. 53 (2020) 226–235, https://doi.org/10.1107/S1600576719014092.

[23] H.S. Yu, X. He, D.G. Truhlar, MN15-L: a new local exchange-correlation functional for Kohn–Sham density functional theory with broad accuracy for atoms, molecules, and solids, J. Chem. Theory Comput. 12 (2016) 1280–1293, https://doi.org/10.1021/acs.jctc.5b01082.

[24] F. Weigend, R. Ahlrichs, Balanced basis sets of split valence, triple zeta valence and quadruple zeta valence quality for H to Rn: design and assessment of accuracy, Phys. Chem. Chem. Phys. 7 (2005) 3297, https://doi.org/10.1039/b508541a.

[25] F. Weigend, Accurate coulomb-fitting basis sets for H to Rn, Phys. Chem. Chem. Phys. 8 (2006) 1057, https://doi.org/10.1039/b515623h.

[26] M.J. Frisch, G.W. Trucks, H.B. Schlegel, G.E. Scuseria, M.A. Robb, J.R. Cheeseman, G. Scalmani, V. Barone, G.A. Petersson, H. Nakatsuji, X. Li, M. Caricato, A. V. Marenich, J. Bloino, B.G. Janesko, R. Gomperts, B. Mennucci, H.P. Hratchian, J. V. Ortiz, A.F. Izmaylov, J.L. Sonnenberg, D. Williams-Young, F. Ding, F. Lipparini, F. Egidi, J. Goings, B. Peng, A. Petrone, T. Henderson, D. Ranasinghe, V. G. Zakrzewski, J. Gao, N. Rega, G. Zheng, W. Liang, M. Hada, M. Ehara, K. Toyota, R. Fukuda, J. Hasegawa, M. Ishida, T. Nakajima, Y. Honda, O. Kitao, H. Nakai, T. Vreven, K. Throssell, J.A. Montgomery Jr., J.E. Peralta, F. Ogliaro, M. J. Bearpark, J.J. Heyd, E.N. Brothers, K.N. Kudin, V.N. Staroverov, T.A. Keith, R. Kobayashi, J. Normand, K. Raghavachari, A.P. Rendell, J.C. Burant, S.S. Iyengar, J. Tomasi, M. Cossi, J.M. Millam, M. Klene, C. Adamo, R. Cammi, J.W. Ochterski, R.L. Martin, K. Morokuma, O. Farkas, J.B. Foresman, D.J. Fox, Gaussian, 16, Gaussian, Inc., Wallingford, CT, 2019. Revision C.01.

[27] P. Geerlings, F. De Proft, W. Langenaeker, Conceptual density functional theory, Chem. Rev. 103 (2003) 1793–1874, https://doi.org/10.1021/cr990029p.

[28] H.-A. Tsai, M.-C. Suen, P.-N. Wang, Y.-F. Hsu, J.-C. Wang, J. Coord. Chem. 64 (2011) 2658–2666, https://doi.org/10.1080/00958972.2011.605123.

[29] N.R. Pereira, M.E. Alvarenga, R. Diniz, R.C. de Santana, L.J.Q. Maia, B.J.G. Dutra, F.F. Guimarães, C.M. da Silva, F.T. Martins, Solid state structural and light emission color diversity from styrylbenzothiazole derivatives, J. Mol. Struct. 1365 (2026) 146043, https://doi.org/10.1016/j.molstruc.2026.146043.
[30] D. Petrova, B. Angelov, Electronic energy levels of lithium gadolinium tetraphosphate ($LiGdP_4O_{12}$), Optik 124 (2013) 6338–6340, https://doi.org/10.1016/j.ijleo.2013.05.056.
[31] M. Farouk, Effect of Co^{2+} ions on the ligand field, optical, and structural properties of ZnLiB glasses, Optik 140 (2017) 186–196, https://doi.org/10.1016/j.ijleo.2017.04.042.
[32] M.G. Brik, N.M. Avram, C.N. Avram, C. Rudowicz, Y.Y. Yeung, P. Gnutek, Ground and excited state absorption of Ni2+ ions in MgAl2O4: crystal field analysis, J. Alloys Compd. 432 (2007) 61–68, https://doi.org/10.1016/j.jallcom.2006.06.025.
[33] S. Som, S.K. Sharma, T. Shripathi, Influences of doping and annealing on the structural and photoluminescence properties of Y_2O_3 nanophosphors, J. Fluoresc. 23 (2013) 439–450, https://doi.org/10.1007/s10895-013-1160-7.
[34] S. Khalid, I. Umer, S.A. Buzdar, A. Majid, N. ul Hassan, S.S. Alarfaji, M.I. Khan, Investigating the dilute magnetic semiconductor behavior of 4d transition metal adsorption on B_4C_3, J. Magn. Magn. Mater. 598 (2024) 172045 https://doi.org/10.1016/j.jmmm.2024.172045.
[35] D. Riegel, K.D. Gross, Magnetism and electronic structure of 3d and 4d ions in metals, Phys. B 163 (1990) 678–682, https://doi.org/10.1016/0921-4526(90)90306-F.
[36] T. Alotaibi, M. Alotaibi, F. Alhawiti, N. Aldosari, M. Alsunaid, L. Aldawas, T. F. Qahtan, A.K. Ismael, Tuning the electronic properties of $CumAg_n$ bimetallic clusters for enhanced CO_2 activation, Int. J. Mol. Sci. 25 (2024) 12053, https://doi.org/10.3390/ijms252212053.
[37] M.R. Dolgos, A.M. Paraskos, M.W. Stoltzfus, S.C. Yarnell, P.M. Woodward, The electronic structures of vanadate salts: cation substitution as a tool for band gap manipulation, J. Solid State Chem. 182 (2009) 1964–1971, https://doi.org/10.1016/j.jssc.2009.04.032.
[38] G. Li, Y. Wei, Z. Li, G. Xu, Synthesis and photoluminescence of Eu^{3+} doped $CaGd_2(WO_4)_4$ novel red phosphors for white LEDs applications, Opt. Mater. 66 (2017) 253–260, https://doi.org/10.1016/j.optmat.2017.02.018.
[39] C.S. McCamy, Correlated color temperature as an explicit function of chromaticity coordinates, Color Res. Appl. 17 (1992) 142–144, https://doi.org/10.1002/col.5080170211.
[40] S. Mizukami, H. Houjou, K. Sugaya, E. Koyama, H. Tokuhisa, T. Sasaki, M. Kanesato, Fluorescence color modulation by intramolecular and intermolecular π–π interactions in a helical zinc(II) complex, Chem. Mater. 17 (2005) 50–56, https://doi.org/10.1021/cm049744s.
[41] H. Bhatia, S. Dey, D. Ray, Effect of π···π interactions of donor rings on persistent room-temperature phosphorescence in D4–A conjugates and data security application, ACS Omega 6 (2021) 3858–3865, https://doi.org/10.1021/acsomega.0c05666.
[42] J.B. Birks, L.G. Christophorou, Excimer fluorescence of aromatic hydrocarbons in solution, Nature 194 (1962) 442–444, https://doi.org/10.1038/194442a0.
[43] Probing the δ-stacking induced molecular aggregation in δ-conjugated polymers, oligomers, and their blends of p-phenylenevinylenes, J. Phys. Chem. B 112 (2008) 1119–1129, https://doi.org/10.1021/jp077404z.
[44] S. Bandyopadhyay, S.K. Kalangi, V. Singh, R.S. Bhosale, Introduction to aggregation induced emission (AIE) materials, Prog. Mol. Biol. Transl. Sci. 184 (2021) 1–9, https://doi.org/10.1016/bs.pmbts.2021.10.001.